Version of Record: https://www.sciencedirect.com/science/article/pii/S0378779619300471
Manuscript_85ccaf50eb0111dac18697f49451f154

Coupling Computational Fluid Dynamics with the High Resolution Rapid Refresh Model for Forecasting Dynamic Line Ratings

Alexander W. Abboud[1*], Kenneth R. Fenton[2], Jacob P. Lehmer[1], Benjamin A. Fehringer[1], Jake P. Gentle[1], Timothy R. McJunkin[1], Katya L. Le Blanc[1], Melissa A. Petty[2], Matthew S. Wandishin[3]

[1] *Idaho National Laboratory, Idaho Falls, Idaho, United States*
[2] *National Oceanic and Atmospheric Administration - Cooperative Institute for Research in the Atmosphere, Boulder, Colorado, United States*
[3] *National Oceanic and Atmospheric Administration - Cooperative Institute for Research in the Environmental Sciences, Boulder, Colorado, United States*

Abstract

This study looks at forecasted dynamic line ratings in southern Idaho by using data from the high resolution rapid-refresh (HRRR) model for forecasted weather conditions. The HRRR model can provide accurate 18-hour forecasts with a 15-minute temporal resolution. Typical static ratings used for overhead transmission lines use overly conservative assumptions for local weather conditions, such as using the maximum solar irradiance and ambient temperature measured during the summer, combined with low wind speed for an entire season. The HRRR forecast model used here has high spatial resolution to provide local forecast conditions along the entire length of a transmission line. The area that is of interest in this study is in southern Idaho, spanning a total of 15,000 square kilometers. The forecasted weather data are coupled with a computational fluid dynamics (CFD) model of the wind in the region for fine-scale resolution of convective cooling rates on the

*corresponding author: alexander.abboud@inl.gov

Abbreviations: computational fluid dynamics (CFD), dynamic line rating (DLR), High-Resolution rapid-refresh (HRRR), numerical weather prediction (NWP), Reynolds-averaged Navier-Stokes (RANS), National Oceanic and Atmospheric Administration (NOAA), National Center for Environmental Prediction (NCEP), general line ampacity state solver (GLASS), systematic analyzer of numerical data (SAND)

midpoint of each individual transmission-line span. This high-fidelity approach can be used to find the minimum ampacity across all given midpoints of a transmission line to determine the limit to be used for the line rating. The ability to increase the overhead line rating above the conservative static approach with the forecasted weather data provides a large potential to alleviate congestion and provide data for utility-market transactions, as well as benefits for wind energy generation through concurrent cooling. This study shows that for the region of interest, using forecasted weather data coupled with CFD modeling can calculate DLR ampacity rating above static over 90% of the time, with a small relative error in the forecasted ampacity over time.

Keywords: Dynamic Line Rating, Computational Fluid Dynamics, Weather Forecasting, Overhead Transmission Lines, High Resolution Rapid Refresh

1. Introduction

The amount of current that is run through an overhead transmission line determines the amount of sag which occurs due to thermal expansion as the temperature increases from the Joule heating effect. The limit for the current is typically determined for a set of assumptions on weather conditions set to either fixed or seasonally adjusted values. This limit is typically highly conservative and often uses the maximum ambient temperature and solar irradiance combined with very low wind speeds. Dynamic line rating (DLR) will instead calculate the limit on the ampacity based on local conditions, while updating this limit as the weather changes, usually providing a much higher current limit on the overhead transmission lines. The DLR method can be used to defer infrastructure upgrades, support transmission network during outages, increase distributed generation yields and has been identified by the U.S. Department of Energy as a key transmission and infrastructure solution [1, 2].

For a steady-state calculation of the DLR, the maximum current is solved using a heat balance on the heat losses from convective flow of the wind and thermal radiation with the heat gains from Joule heating and solar irradiance. The equation used for the DLR calculation is the same used in the standard models for overhead-line capacity from the Institute of Electrical Engineers standards [3, 4], and aligns with the International Council on Large Electric

Systems [5–7] and the International Electrochemical Commission [8]. The maximum temperature of the conductor is determined through the allowable amount of thermal expansion of a given conductor to avoid clearance issues from sagging between two pole structure locations.

Typical static ratings use conservative estimates for calculating the limit for overhead transmission lines, though some may contain adjustments such as ambient adjusted ratings. For example, static conservative assumptions used by power companies may be 40°C, wind speed of 0.6 m/s, wind direction parallel to the midpoint azimuth, and solar flux of 1030 W/m^2 [9]. Utilizing DLR can increase the ampacity of overhead conductors while avoiding the issues associated with high temperature on conductors, such as line sag or annealing at extreme temperatures. Several case studies utilizing observed real-time weather data throughout various regions in Canada [10, 11], the US and the UK [12–14], as well as locations in France [15], Spain [16], Italy [17], South Korea [18] have shown potential for the increase in ampacity of transmission lines using DLR. Other studies into DLR have shown potential for day-ahead planning [19], or as a way to ease congestion of overhead transmission lines [20, 21]. Another area to benefit from DLR methodology is the natural synergy with increased wind power generation, coupled with higher convective cooling from the wind [22–29].

For the current state of DLR, the primary approaches are divided into two main categories: monitoring the conductor's physical parameters directly and the environmental parameters that affect line rating calculations [30, 31]. Direct-conductor monitoring sensors can measure the temperature and use other parameters, such as sag, tension, and clearance, to provide measurements that can be used to calculate the conductor temperature and the effective wind, used to arrive at the amapcity limit. Generally, direct-conductor monitoring offers great accuracy and precision, but involves challenges from installation and maintenance costs associated with adequately covering enough of the midpoints of a transmission line, along with calibration issues when the load is low [32]. Indirect calculations, using environmental-parameter monitoring of wind speed, direction, and solar irradiance in the heat balance equation, directly to get conductor temperature and ampacity limtits may be more cost-effective, but can be limited in accuracy by the location of weather stations. Both categories of approaches can be used in combination to complement one another, and while these technologies and approaches have been verified in practice, no approach for accuracy and cost determination has been standardized [32]. Some research

in real-time weather-based indirect methods compared to direct measurement of conductor temperatures has shown reasonable validation [33].

Indirect methods can suffer from more uncertainty in the line's loadability so that upper and lower bounds of the ampacity should be calculated with probabilistic methods [34]. Adaptive, synchronized sensor systems, outlined in [35] and expanded on in [36], provide for real-time monitoring of wide areas without the need for conductor-temperature measurement sensors. The sensors can be utilized with an approach to compensate for errors and minimize noise for minimal error in temperatures. Knowledge of voltage and current synchrophasors at the line ends can be used to estimate the temperature with good agreement to two on-conductor temperature-measurement systems [37]. However, this technique for simultaneous parameter identification and measurement calibration has been introduced to address the issue of overhead line parameter monitoring. The series and shunt-line parameters are recursively estimated from the phasor measurements and weather conditions by using an extended Kalman filter. The drawback of this approach is that the use of a standard thermal model [3] requires the acquisition of meteorological variables along the whole transmission-line route nullifying the huge advantage to employ only synchrophasors at the overhead line ends, though automatic identification of faulty sensors is noted as an advantage of the system [35]. The accuracy and reliability of DLR is critical to successful deployment, but inaccuracies can arise through both measurement and modeling errors [38]. Measurement errors can include imprecise or inconsistent measurements and improperly calibrated direct-measurement sensors, as well as periods of light load [39]. Modeling errors encompass inaccurate mathematical rating models, weather-forecasting errors, and errors in collecting circuit topological and conductor data.

However, most real-time DLR methods are not directly applicable to turn into a forecasted DLR method. Some strategies have employed a mathematically described confidence level within the DLR calculation, which rates the power line more conservatively in proportion to lower confidence parameters such as weather predictions [40], or using probabilistic methods to increase confidence in numerical weather predictions (NWPs) [41, 42]. The variability in NWP for use in DLR ampacity has led to a slow deployment of the technology [43]. Some studies point out that in practice the error in NWP can require a scale back of ampacity ratings to deal with inaccuracies in a conservative manner. In extreme cases, the wind and solar data are completely ignored, and day-ahead DLR forecasting utilizes only temperature

[44]. Other studies derate the transmission line ampacity itself with the lower percentiles of the uncertainty bounds [45, 46], while another study utilizes machine learning to improve accuracy for medium resolution NWP for DLR [47].

The method that is outlined here has two main benefits compared to direct-sensor approaches. First, the method is relatively cheap because all the data needed is readily available, and the CFD used is minimal in expense compared to direct sensors. Second, by using CFD to interpolate local wind conditions based on the terrain, the full end-to-end midpoint ampacity values of the entire transmission line can be calculated — a prominent solution to wide-area monitoring issues. Though it should be noted, initial validation of the weather data will require some field-based equipment, and using a pure model-based method carries inherent risks to be assessed.

For large-scale wind simulations in this study, the steady-state Reynolds-averaged Navier-Stokes (RANS) approach is used [48] because the computational time is much more manageable over large terrain scales of interest than other methods, such as large eddy simulation. The WindSim CFD software has been utilized for the calculation of wind fields using RANS turbulence modeling and has been validated in complex terrain [49]. WindSim software has been shown to be more effective in wind speed-up prediction ratios over hilly terrain than the RANS model utilized by the OpenFOAM CFD software [50]. Wind-speed accuracy with RANS flow has been tested by Milashuk and Crane [51] by transforming measurements at a reference location to other locations of interest, and similar wind mapping has been completed on low-elevation mountains by Dhunny et al. within acceptable validation error [52, 53]. Comparing lookup tables created with RANS CFD simulations in relation to actual weather-data observations has also shown acceptable agreement in this same geographic region [12]. The convective-cooling rate is calculated as a function of the Reynolds number raised to the power of 0.52 or 0.6, so an approximate 10% error in wind speed in the simulations translates to about 5% error in the convective-cooling rate. Effectively, any error in wind speed occurring through the CFD modeling translates roughly to a $\Delta Re^{1/4}$ error in ampacity. Coupling weather data with CFD simulations will provide a more conservative estimate for DLR because it accounts for wind speed slowdown due to local terrain.

The weather forecasts used in this study came from version 2 of the high-resolution rapid-refresh (HRRR) model. HRRR is a convection-allowing forecast model that outputs meteorological variables on a 3-km horizontal

grid over the continental United States [54, 55]. The HRRR was developed at the National Oceanic and Atmospheric Administration (NOAA) Earth System Research Laboratory and is run operationally at the National Center for Environmental Prediction (NCEP). The current version of the HRRR, Version 3, became operational on 12 July 2018 and outputs forecasts from zero through 18 hours with 15-minute temporal resolution that are updated every hour. The model also outputs forecasts from zero to 36 hours with one-hour temporal resolution at 00, 06, 12, and 18 UTC. The previous version of the HRRR, Version 2, was operational during the period of this study and was used to provide the temperature, solar-flux, wind-speed, and wind-direction forecasts for the line rating calculations.

This paper first goes over the method for calculating DLR with a look at the sensitivity of DLR to various weather conditions. Next, the methodology used for the CFD results, the HRRR forecast data, and the general line ampacity state solver (GLASS) software are described. This is followed by results that first describe the weather accuracy of the HRRR model in relation to installed weather stations, then describe the CFD wind fields, and finally calculate the dynamic line rating using GLASS coupled with the CFD results and the HRRR-forecasted weather data. The forecasted ampacity data are analyzed over a year-long time span with respect to the seasonal static rating of the line.

1.1. Trial Site Description

The site of interest is a region 15,000 km^2 that spans from the Boise metro area to the Twin Falls area in Idaho. The elevation of this area is shown in Figure 1a, along with the roughness layer in Figure 1b. The roughness layer is a representation of local near-ground change, such as buildings, trees, or shrubs in the terrain. In order to handle the computational load, the region is split into four sub regions, which are along the corridor of the power line. These four sub-domains are shown in black outlines in Figure 1a, labeled as NW2, NW1, Central, and East sections.

2. Methodology

2.1. Overview

A case study of using the methodology within a specific geographical region on a single transmission line of interest is presented. However, the

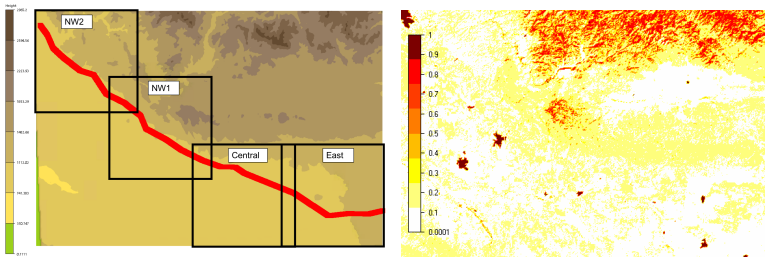

(a) (b)

Figure 1: (a) Elevation of the terrain with the singular transmission line that is examined with sub-domains drawn for CFD calculations, and (b) roughness layer of the terrain. Light colors refer to flatter regions, while red and dark red are forests and cities, respectively

method proposed in this paper can be broadly applied to any line configuration using various types of weather forecasts. The first step is to select the weather forecast, which can be from a weather model such as the HRRR or human-in-the-loop weather forecasts from the National Weather Service. The NCEP runs many different weather models at various resolutions that are publicly available through the NOAA Operational Model Archive and Distribution System. The variables of two-meter temperature, ten-meter wind speed, ten-meter wind direction, and surface radiation flux are used from the desired weather forecast source for the forecast time. To analyze how much the weather conditions can change over time the long-term (in this case 18-hour ahead) forecasts can be directly compared to the near-term forecasts for determining the confidence of how they may shift over time. This is done for both the individual weather conditions, as well as the total calculated ampacity. In order to mitigate risk, this comparison can also be done against observed weather data, and the calculated ampacity from those values to determine how much the forecast ampacity can deviate from the actual ampacity. Derating the amapcity by standard deviations of the changing forecast is demonstrated as an example risk mitigation.

Next, a section of overhead transmission lines is identified in the region of interest. The extent of the terrain around the overhead transmission lines for the CFD model is determined. To avoid boundary-condition effects the terrain extent should have sufficient room between the edges of the modeled terrain and the transmission-line structures. The horizontal resolution of the CFD should be as resolved as possible within the computational limits available, though 30 meters may be the limit in some regions based on available

digital elevation model data. If the extent of the terrain is too large, the domain can be decomposed to run several different CFD simulations. Each midpoint span is matched to its nearest weather forecast point. The weather data at each midpoint span are then entered into the line-rating equation with the line parameters and a maximum conductor temperature to output the maximum amount of current that can be transmitted through the conductor at the midpoint. When coupling with the CFD portion, wind data are first passed through lookup tables to adjust wind speed and direction according to local terrain effects. For solar flux and temperature data, values are assumed to be the same as the nearest NWP model point. The minimum calculated current value from among all the transmission-line midpoints is then selected as the maximum current that can be conducted through the section of line without exceeding the maximum conductor temperature.

2.2. Steady-state Dynamic Line Rating Calculations

The overall equation for solving the steady-state line rating is a heat balance between Joule heating, solar irradiance, radiative heat loss and convective cooling, given by

$$I^2 R(T_c) + q_s = q_c + q_r \tag{1}$$

where q_s, q_c, and q_r are heating though solar radiation, cooling through convection, and cooling through radiation; T_c is the core temperature of the conductor, I is the current, and R is the resistance of the line. $I^2R(T_c)$ is the internal heating due to the current from the Joule heating effect.

For the forecasted dynamic line rating, the steady-state value is updated in the frequency of the HRRR model with 15-minute intervals. Wind speed is only one piece of the calculation. Other environmental factors are accounted for — namely, the solar irradiance, ambient temperature, and wind direction. The equations and methodology are documented in IEEE standard 738 [3]. In order to solve for the steady-state current capacity, the heat-balance Eq. (1) is used to solve for the current, I, to get

$$I = \sqrt{\frac{q_c + q_r - q_s}{R(T_c)}} \tag{2}$$

The radiated heat loss rate per unit length of the transmission line in units of W/m is calculated by

$$q_r = 17.8D\epsilon \left[\left(\frac{T_c + 273.15}{100} \right)^4 - \left(\frac{T_a + 273.15}{100} \right)^4 \right] \tag{3}$$

where ϵ is the emissivity, D is the conductor diameter and T_a is the ambient air temperature in Celsius. In the normal standards, the heat gain from the sun through solar irradiance is calculated by

$$q_s = \alpha Q_{se} \sin(\theta) A' \tag{4}$$

where α is the solar absorptivity, Q_{se} is the total solar- and sky- radiated heat flux corrected by elevation, θ is the effective angle of incidence of the sun's rays and A' is the projected area of conductor per unit length. The convective heat loss per unit length is calculated using one of two equations, based on wind speed. For low wind speed, i.e. under 1.34 m/s (3 mph), the term is given by

$$q_{\mathrm{c1}} = \left[1.01 + 1.35 \left(\frac{DV_w \rho_f}{\mu_f} \right)^{0.52} \right] k_f K_{\mathrm{angle}} (T_c - T_a) \tag{5}$$

and for higher air speed, the convective heat loss is given by

$$q_{\mathrm{c2}} = 0.754 \left(\frac{DV_w \rho_f}{\mu_f} \right)^{0.6} k_f K_{\mathrm{angle}} (T_c - T_a) \tag{6}$$

where V_w is the speed of the air, K_{angle} is the wind-direction factor, and the fluid parameters density, ρ_f, viscosity, μ_f, and thermal conductivity, k_f, are calculated at the film temperature. Due to the high variability of the terrain, air density is calculated as a function of elevation as well, and the parameter can vary as much as 20% when comparing areas at elevation to sea level. The wind-direction factor is based on the angle between the wind direction and the conductor azimuth for each midpoint segment as

$$K_{\mathrm{angle}} = 1.194 - \cos(\phi) + 0.194 \cos(2\phi) + 0.368 \sin(2\phi) \tag{7}$$

where ϕ is the angle of incidence between the wind direction and the midpoint azimuth, with maximum value of 90 degrees. The convective cooling rates are compared to the natural convective heat-loss rate given by

$$q_{\mathrm{cn}} = 3.645 \rho_f^{0.5} D^{0.75} (T_s - T_a)^{1.25} \tag{8}$$

the highest of the heat loss rates is used as q_c in the equation for the ampacity for each timestep. These calculations are repeated for every midpoint in the region. For a transmission line, only the lowest midpoint value of the steady-state calculation at that time stamp is used to determine ampacity. Lookup tables are created for each midpoint using the WindSim code, and these lookup tables are fed together with the archived HRRR forecast data through the GLASS code developed by INL to determine the ampacity. Because the wind near ground level is a boundary-layer flow, the results should be self-similar so that, for each wind direction, one simulation can give an effective solution that is then scaled by real-time conditions. The methodology here is applied to archived HRRR weather data, but should be applicable for actual forecasted data with only minor application programming interface development [43].

2.3. Sensitivity of Dynamic Line Rating to Weather

Single-variable sensitivity tests are run to examine the dependence of line rating on each of the weather variables. For each sensitivity plot, other variables are held constant at values, with an ambient temperature of 21 °C, 0.0 solar flux, 0.0 wind speed, and perpendicular used as a control setting. The sensitivity for all four of these variables over the ranges of interest are shown in Figure 2(a-d) for , solar irradiance, ambient temperature, wind direction and wind speed, respectively.

Wind speed shows the largest change of all of the variables, with the sensitivity value changing the total ampacity calculation by 2300 A over the range of values. The second most important parameter is wind direction, which can change the ampacity by 900 A over the range of the calculated values. Solar irradiance and ambient temperature have roughly the same impact on the ampacity calculation over the ranges, with a variation of only 200 A. In some cases, ambient-adjusted ampacity ratings rely on the local temperature variations from day to day. The sensitivity plot over the ambient temperature shows this is not so impactful a variable, as variations from the middle of summer to the middle of winter are quite small, and day-to-day variations would be significantly less than 200 A.

It should be noted that wind direction has a strong cross-correlation effect with wind speed. At higher wind speeds, the direction of the wind has a larger impact on the ampacity calculation. This is due to the K_{angle} term in Eq. (7) applied as a multiplier to the convective heat-loss rate. The multiplier is plotted in Figure 3a, and the impact this has on the wind speed of a

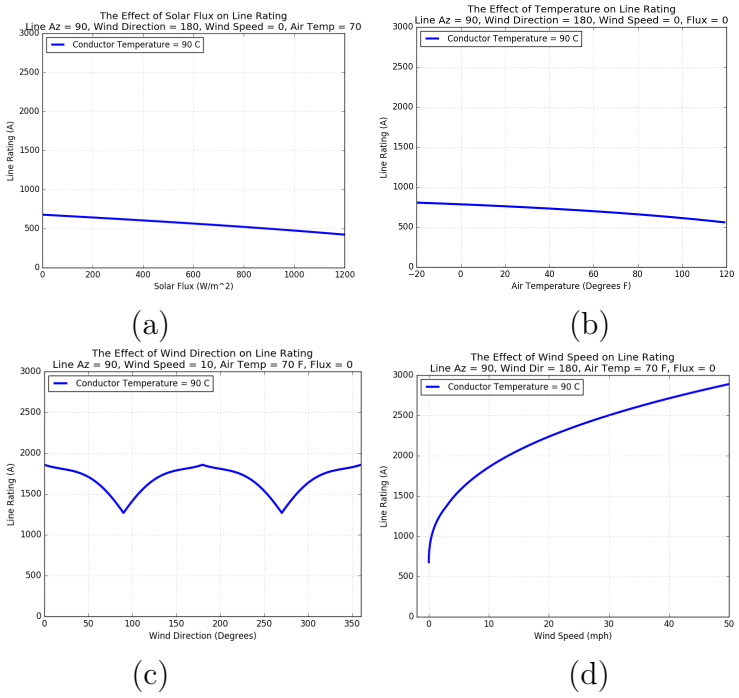

Figure 2: Single-variable sensitivity for (a) solar irradiance (b) ambient temperature, (c) wind direction, and (d) wind speed with other variables held constant.

perpendicular versus parallel wind flow is shown in Figure 3b. At higher wind speeds, the variation of the ampacity calculation increases more than at low speeds. These sensitivity plots all point to the wind as the most impactful weather condition on dynamic line rating, which validates the importance that is placed on CFD to resolve the wind fields in this study.

2.4. Computational Fluid Dynamics

The partial differential equations dictating the wind-field solution for the RANS model with the standard $k-\epsilon$ method are well defined. These are the three velocity vectors, U_i, the turbulent kinetic energy, k, and the turbulent dissipation rate, ϵ, given by:

$$\rho U_i \frac{\partial U_j}{\partial x_i} = \frac{\partial}{\partial x_i}\left[(\mu + \mu_t)\left(\frac{\partial U_i}{\partial x_j} + \frac{\partial U_j}{\partial x_i}\right)\right] - \frac{\partial p}{\partial x_i} \tag{9}$$

for the three velocity vectors,

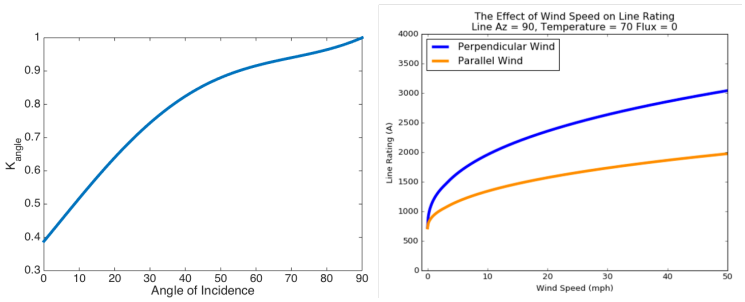

(a) (b)

Figure 3: The (a) variation of the K_{angle} term with respect to the angle of incidence of the wind and (b) the change in ampacity with wind speed of a parallel angle of incidence compared to a perpendicular angle of incidence (b).

$$\frac{\partial(U_i k)}{\partial x_i} = \frac{\partial}{\partial x_i}\left(\frac{\mu_t \partial k}{\sigma_k \partial x_i}\right) + P_k - \epsilon \tag{10}$$

for the turbulent kinetic energy,

$$\frac{\partial(U_i \epsilon)}{\partial x_i} = \frac{\partial}{\partial x_i}\left(\frac{\mu_t \partial \epsilon}{\sigma_\epsilon \partial x_i}\right) + c_{\epsilon 1}\frac{\epsilon}{k}P_k - c_{\epsilon 2}\frac{\epsilon^2}{k}P_k \tag{11}$$

for the turbulent dissipation rate. In these equations the turbulent viscosity, μ_t, is given by:

$$\mu_t = \frac{C_\mu k^2}{\epsilon} \tag{12}$$

and the turbulent production term, P_k, is given by:

$$P_k = \mu_t\left(\frac{\partial U_i}{\partial x_j} + \frac{\partial U_j}{\partial x_i}\right)\frac{\partial U_i}{\partial x_j} \tag{13}$$

where c_μ, $c_{\epsilon 1}$, $c_{\epsilon 2}$, σ_k and σ_ϵ are the fixed constants for the $k-\epsilon$ model, with values set to 0.09, 1.55, 2.0, 1.0 and 1.3, respectively [48]. The terrain of interest spans a 15,000 km^2 region. In order to effectively compute the wind fields in this region, the terrain is divided into four sectors of 40 km by 40 km along the transmission line of interest. The effective spatial resolution is 40-meters in the horizontal direction. In the vertical direction, 5-meter grid spacing is used near ground level up to 50 meters, with 10-meter spacing up to 100 meters, and logarithmic spacing up to the atmospheric boundary

layer. This captures the near-ground wind flow with more accuracy at the heights of interest for the transmission line midpoint spans.

2.5. High-resolution Rapid-refresh Model

This study compared line ratings calculated using weather data from both the HRRR forecasts and weather-station observations colocated with power lines in southwestern Idaho. Figure 4a and Figure 4b provide zoomed in views that show the relative densities of the 3-km HRRR grid points and the weather stations, with Figure 4b corresponding to a zoomed subsection of Figure 4a. Each weather station was matched to its nearest HRRR grid point to create a proxy set of weather conditions based on the HRRR forecasts. Forecasts from the HRRR points were then input into GLASS to get the line ampacity.

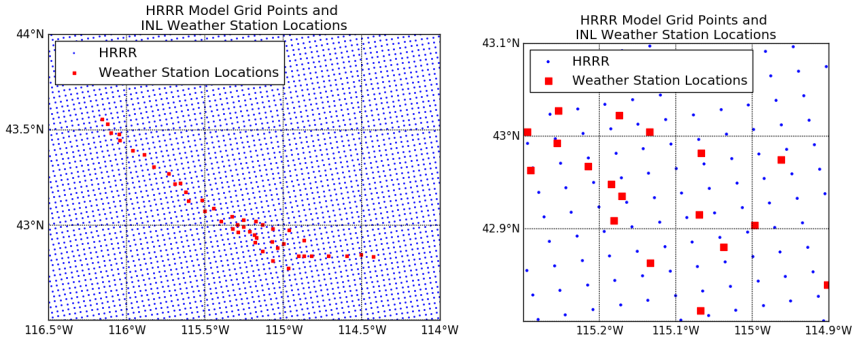

(a) (b)

Figure 4: The full HRRR domain that covers the region of interest in Idaho (a) a view of the 3-km HRRR grid points and the weather-station locations and (b) a zoomed in view showing the relative densities of the HRRR grid points and the weather stations.

2.6. General Line Ampacity State Solver

The program referred to as GLASS is used for the analysis of the archived HRRR data in combination with CFD-generated data from WindSim. Figure 5 shows the high-level algorithm utilized by GLASS for generating weather-based DLR ratings for either real-time or forecasted weather data. The main components that are used in the analysis presented in this paper are the CFD portion, which utilizes the WindSim CFD code, the Systematic Analyzer of Numerical Data (SAND), used for processing the HRRR archived weather

data of wind speed, wind direction, solar irradiance, and ambient temperature into a database, and GLASS, which solves the equations in Subsection 2.2 for every database entry to calculate final values for the ampacity rating. An advantage of GLASS is that it has been built in such a way that it can provide ampacity estimations for every midpoint span along numerous line sections simultaneously, while also allowing for time-syncing of weather data from any source.

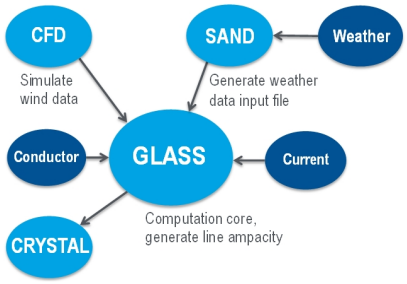

Figure 5: Representation of the data flow through the GLASS code.

While the subject is not addressed in this study, the GLASS software is capable of handling both weather measurement data and direct-sensor readings, with a natural synergy arising from the weaknesses present in both data types. When weather data is used the state of the transmission line may have some error associated with local conditions. When direct-measurement data is used the state of the local weather conditions requires assumptions to calculate, and typically combines the wind cooling conditions so that it may not be applicable to the next line segment if the azimuth varies. GLASS can resolve the data from direct and indirect methods together to give a more reliable ampacity across multiple spans.

3. Results and Discussion

3.1. Wind Flow Fields

The wind data that are of relevance to overhead transmission lines is 10-meter above ground level, where most midpoint spans are located. In Figure 6, the wind fields for the four sectors are shown with northern incoming wind. When subjected to northern wind flow, the regions in the mountains are most affected by the wind. However, along the foothills where the transmission lines are located, the wind patterns show slowing effects from the terrain as

well. The other incoming wind sectors are shown in Figure 7, Figure 8, and Figure 9 for eastern, southern and western incoming wind speeds, respectively. When the wind is coming from the east, it impacts a slowdown from the mountains on the northwest two sectors, but the sectors which are southeast and central see higher wind speeds throughout the region. When the wind is incoming from the southern and the western directions, simulations show the smooth incoming terrain does not slow the wind as much, resulting in higher wind speeds. Throughout the contour plots, the scale runs from 0 to 10 m/s. It is assumed that the atmospheric boundary-layer speed is at 10 m/s (the boundary layer speed has negligible effects on wind speed-up and direction-shift model predictions [49]). It is also assumed that the large-scale wind-low patterns would not shift drastically at higher wind speeds so that the flow patterns are self-similar. Using this wind-speed simulation data, the relative wind speed and directional shift between each HRRR-to-midpoint mapping is calculated. When processing the GLASS data, the weather data are then multiplied by the appropriate wind speed shift to determine speed at each midpoint span. Correspondingly, the direction shift is added (or subtracted) to the weather data to determine wind direction at each midpoint. There exists a wind-speed and wind-direction shift specific to each of the 12 incoming wind sectors of the simulations.

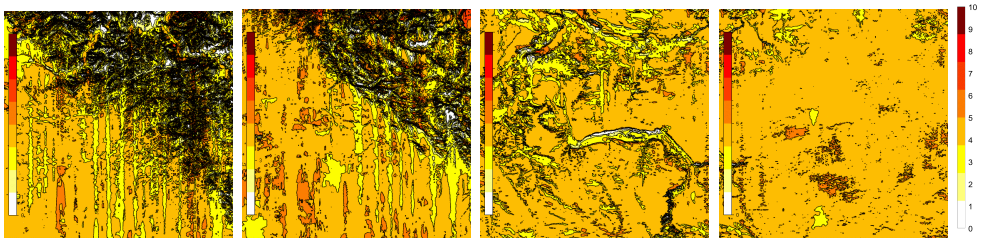

Figure 6: Ten meter height wind fields for the northern incoming wind, with units of m/s for (a) NW1, (b) NW2, (c) Central and (d) East subsections.

In addition to the plots at 10-meter data, the CFD wind fields can be used to examine data further above the ground. This shows the extent of the boundary layer of the flow. As the height is increased, the impact of the ground is decreased, and wind speeds increase. In addition, the impact of the mountains on the wind flow will also decrease, but at 100-meters will still be noticeable. This impact of the height on wind-field flow is highlighted for

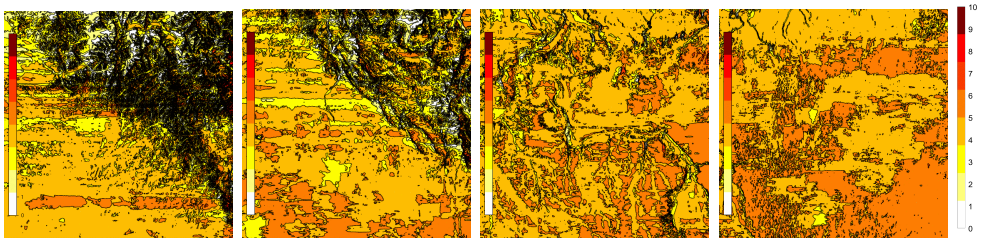

(a) (b) (c) (d)

Figure 7: Ten meter height wind fields for the eastern incoming wind for (a) NW1, (b) NW2, (c) Central and (d) East subsections

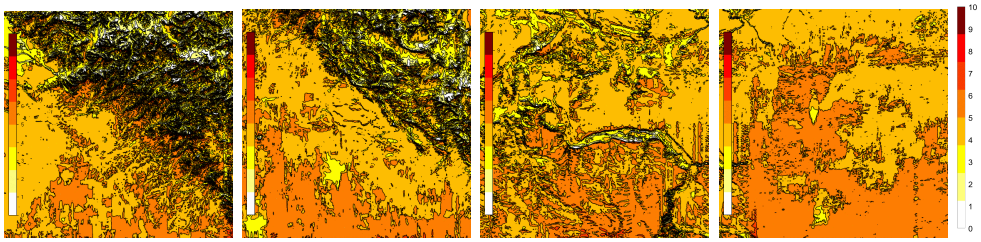

(a) (b) (c) (d)

Figure 8: Ten meter height wind fields for the southern incoming wind for (a) NW1, (b) NW2, (c) Central and (d) East subsections

the northern direction in the northwest-1 sector of the wind field in Figure 10. The increase in wind speed is quite significant, moving from 10-meter heights to 100-meter heights above ground level.

3.2. HRRR Weather Comparison

The error of the HRRR model measured against weather station observations is shown in Figure 11 for each of the four weather components of interest. For a simplistic comparison, the HRRR data are compared to a persistence assumption, where persistence is defined as forecasting the current value of a weather parameter to continue indefinitely into the future. In the near term, under 2.5 hour forecasts, the persistence assumption does outperform the HRRR model; however, due to the delay time in the HRRR model calculation and data availability, this time period is not of concern within the context of this analysis. It is noted that persistence assumptions should be used in the short term (less than 2.5 hours), but not in day-ahead estimations of DLR. For forecasts three hours and beyond, the HRRR model

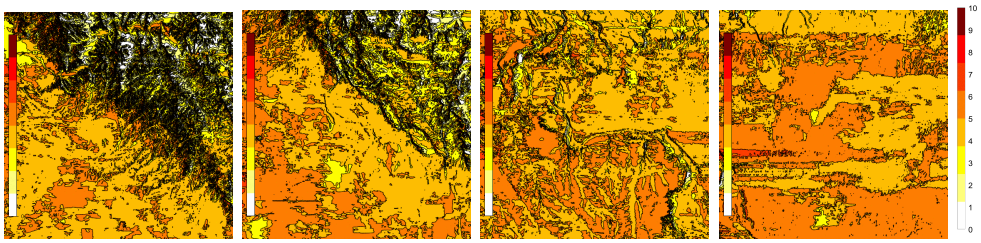

Figure 9: Ten meter height wind fields for the southern incoming wind for (a) NW1, (b) NW2, (c) Central and (d) East subsections

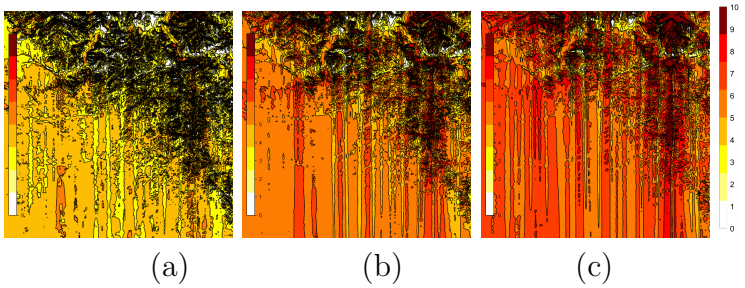

Figure 10: The (a) 10- (b) 50- and (c) 100- meter height above the ground level wind fields for the southern incoming wind

shows significantly less error than the persistence assumption for all four of the weather conditions of interest. In addition, it is seen that changes in the HRRR forecasted error are only minor with increased time ahead in the forecast. This potentially allows for a similar confidence in using the long-term 18-hour forecasts, as one would have in shorter term forecasts. The summary of this error in terms of the root mean square error (RMSE) quantities for the forecast hour 3 is shown in Table 1.

The RMSE for the ambient temperature is rather minor and, as shown in Figure 2b, this small error in the temperature would have only a minor impact on calculated ampacity. Similarly, the solar irradiance value is relatively small compared to the possible range, and due to the small slope of the sensitivity plot in Figure 2a, would not have much impact on calculated ampacity. The RMSE in the wind speed may have a significant impact at low wind speeds in the ampacity calculation, but at higher wind speeds, the slope of the sensitivity levels off and becomes less important. The wind direction may also be of concern in the error of the forecasts. While at high

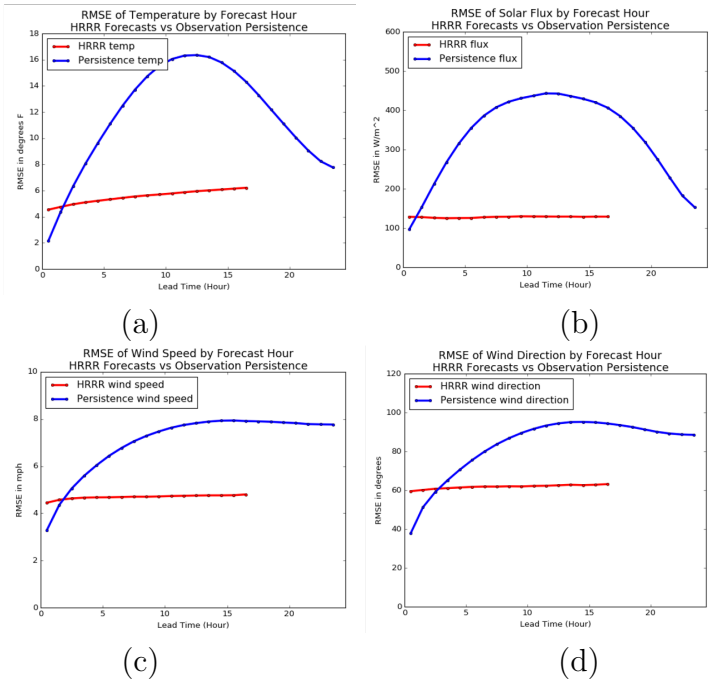

Figure 11: Root mean square error of the HRRR forecasts compared to persistence, the period of interest past the third future hours is highlighted for (a) the temperature, (b) the solar ampacity, (c) the wind speed and (d) the wind direction.

angles of incidence (above 50 degrees), wind direction has a relatively minor effect on calculated ampacity, due to the K_{angle} term plotted in Figure 3a. However, at a low angle of incidence, there is much more uncertainty in the calculated ampacity due to wind-direction change. This is reflected in the sensitivity plots to a 0 degree line by the shallow peaks around 0 and 180 wind direction, and the sharp valleys around 90 and 270 degree wind direction, in Figure 2c.

3.3. Ampacity Calculations

All collected HRRR data are reformatted through the SAND code for input into the GLASS code. The GLASS code then outputs the steady-state ampacity for every time step in this year-long analysis. This was done using two different assumptions, due to the fact that data pulled from the HRRR archive could sometimes be incomplete. The first assumption was that during missing data points, the data were consistent in the near-term, so that a persistence assumption was used until a new data point occured. Second,

Table 1: The RMSE values of HRRR model point error compared to the nearest weather station, at forecast hour 3.

Measurement	**HRRR Model Points RMSE Values**
Wind Speed	4.57 MPH
Wind Direction	60.1 degrees
Solar Irradiance	127.68 W m^{-2}
Ambient Temperature	4.75°C

data were simply ignored at timestamps weather data was not in the archive as a limiting calculation when doing the calculation of the overall ampacity of this line. These two methods are shown in Figure 12a and Figure 12b, respectively. In the subsequent plots, FC# is the forecasted data for the # hour. When looking at the ampacity with the persistence assumption, it is often seen data is clipped to a fixed value for long periods of time — in particular near the end of the study as data from one model point is missing, and the persistence assumption clips the ampacity significantly in Figure 12a. This may be occurring when a near-zero wind condition is forecasted, then carried through with persistence for a long period of time. Due to this issue, when utilizing the HRRR archived data, using the second assumption to ignore data in calculations may be a better alternative than using a persistence assumption. To demonstrate the sensitivity of the ampacity to wind direction assumptions, the year-long ampacity was also plotted against the static rating calculated when using a parallel wind-flow assumption, Figure 12c (in similar to overall wind patterns in the region in comparison with the line of interest), which shows the significant change in head room. The rest of the analysis uses the conservative parallel rating as static.

The ampacity predicted using the HRRR model data for different forecast hours is shown in Figure 13 for 3, 10 and 18 hours in the future. These data fix the forecast hour to create a time series of all forecasts at that forecast hour for the entire data period. This may be the equivalent of a utility planner always using a specific hour for near- and long-term estimations of the ampacity on a given transmission line. While differences occur in some of the peaks and valleys in predictions across the year-long span, overall the data show very similar trends, with large amounts of ampacity above headroom in the summer, and slightly less in the winter. Each time the static rating is crossed by the DLR rating lies in the seasonal-change saddle

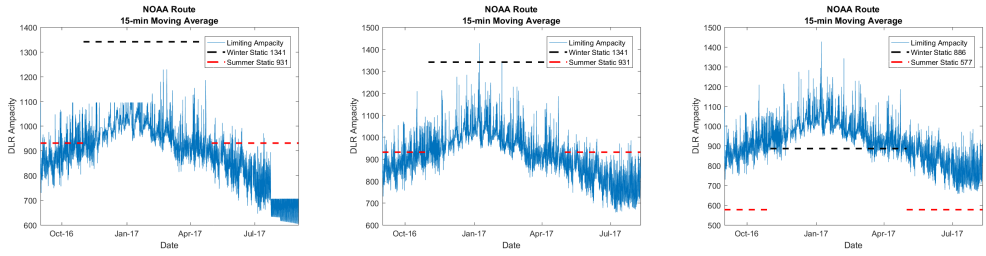

(a) (b) (c)

Figure 12: The calculated ampacity compared to the winter, summer, and static ratings for this line (a) using persistent data when unarchived data is seen, (b) ignoring timestamps when unarchived data is seen, and (c) plotted against a parallel wind assumption for static rating.

in spring and fall months before the hard switch of the seasonal static rating occurs.

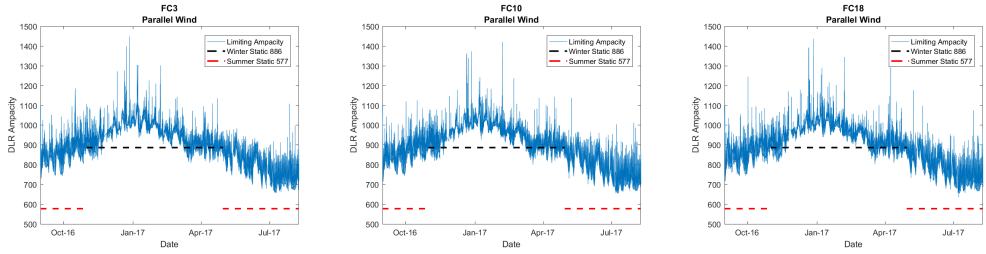

(a) (b) (c)

Figure 13: Raw ampacity calculations compared to the static summer and winter ratings for (a) forecast hour 3, (b) forecast hour 10 and (c) forecast hour 18.

To look at the amount of overall improvement for this line, data from Figure 13 was processed as a histogram of the amount of time DLR ampacity is above static ampacity, as shown in Figure 14. The saddle periods in spring and summer, when the DLR ampacity is occasionally less than the static seasonal ampacity, are highlighted during the winter data in the histogram plot. The amount of time that the forecast ampacity is less than static rating is approximately 90% of the total time in winter.

Ampacity that was calculated for every hour of the forecast was compared to the near-term ampacity rating, which was calculated from the 3-hour forecast. The overall difference in this consistency between forecasts was plotted as a function of the future forecast hour. This change in the forecasted

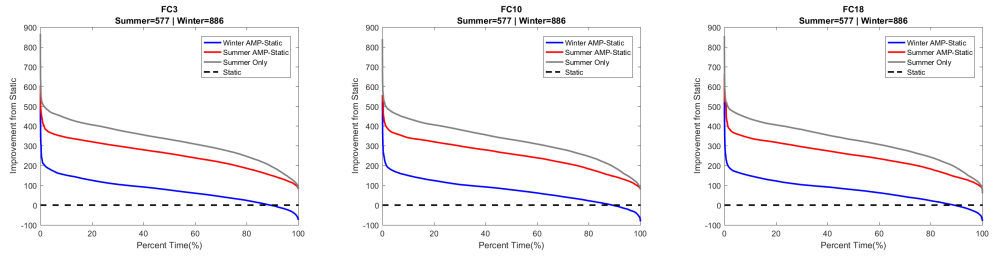

(a) (b) (c)

Figure 14: The amount of time that the calculated DLR rating is above the static rating for (a) forecast hour 3, (b) forecast hour 10, and forecast hour 18.

ampacity as a function of the forecasted hour is shown in Figure 15, which shows the largest increase in error in the early predictive hours from 3 to 4 and 4 to 5. Over the length of the forecast, the gradient of this error decreases as the forecasted time increases.

This type of estimate may give utility planners confidence as to how much additional capacity they can utilize during periods of high line congestion. The maximum error reached at the forecast hour 18 is about 18 A, measured as a raw difference and potentially a small percent difference depending on the line rating. This plot also isolates the average difference only when the error is negative, representing the ampacity lost due to changing conditions. This error essentially shows the possible difference that could occur using the FC18 forecast in the future, with a decreasing ampacity as that future hour is reached due to changes in the forecasted weather. This only raises the difference from the near term forecast up to 19 A. Derating the future forecast by the average error of the available ampacity, 19 A, out of a total 600 to 900 A is insignificant (2 to 5%), and should not deter the use of forecasting for DLR calculations. Based on the calculation of the ampacity above static shown in Figure 14, the ampacity calculated during summer months, when congestion can be more prevalent, are nearly never below the static rating, so this error associated with forecasted ampacity would not be expected to influence curtailment of typical values. Figure 15 also shows the standard deviation of this error, which only increases to 28 A by forecast hour 18, which again is minimal compared to the static rating of this line. More conservative deratings of the forecasted ampacity could utilize the average minus one standard deviation of the forecast, or the average minus three standard deviations for 99.7% coverage of the error, assuming a Gaussian

distribution, but this is left to the utilities.

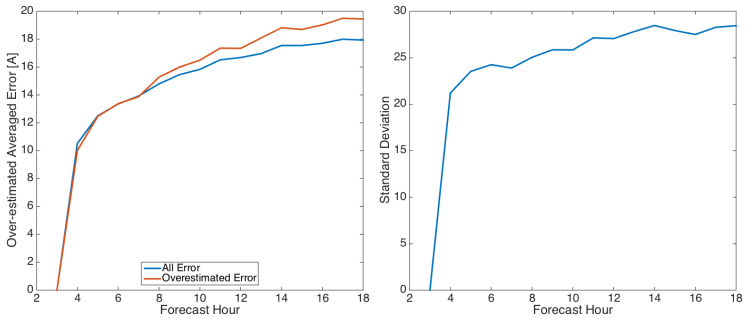

(a) (b)

Figure 15: The (a) normalized change in the ampacity prediction when comparing the longer0term forecasted hours to the near-term forecasted hour, and the standard deviation of the change in the ampacity prediction.

The total amount of time for which long-term forecasts may deviate from short-term forecasts is plotted as a percentage of time over the year in Figure 16a. The amount of time that these large errors could possibly occur between the long-term and the near-term forecasts is well under 1%. During the course of this year-long study, 90% of the time, the 18-hour future forecasts are under one standard deviation of error (28 A) from the near-term forecast hour 3.

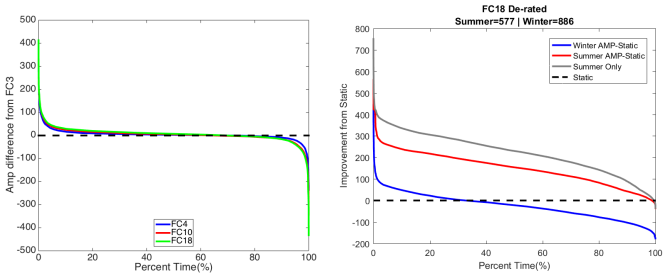

(a) (b)

Figure 16: (a) Amount of time the long-term forecasted ampacity is above or below the near-term forecasted ampacity, (b) the ampacity improvement over the static rating when derating the line by four standard deviations.

There is a small fraction of time, under 4%, where the long-term forecasting hours overestimate the ampacity that is available from the near-term

forecasted hour by a significant amount (25 to 100 A). During this time, the longer-term forecasted ampacity may have an error ranging from one to almost four standard deviations from the near-term forecasted ampacity. During times when deviations from the near- and long-term forecasts occur, the system should be monitored closely if it is operating near the maximum ampacity. As an overly conservative estimate, to make sure the actual ampacity of the line is not overextended through using forecasted data, one could derate the forecasted ampacity by four standard deviations ($\sim$100 A for this line). The result of doing this is shown in the plot in Figure 16b. This shows that even with derated line ampacity to account for the standard deviation in the forecasted ampacity, there is still significant headroom when using DLR calculations during summer months while, during winter months, this conservative derating may only allow for an increase in ampacity 50% of the time. However, winter months typically have little congestion in the region.

Dynamically changing the line rating based on weather forecasts does present risks to the transmission planners. As is shown in Table 1, weather forecasts have a certain amount of error on average. The method proposed here sought to mitigate the forecast error by selecting a 98th percent threshold that should not be exceeded based on recent historical forecast comparisons. Better thresholds, binning of forecasts, and scenario-based methods may be developed to improve the safety factor. In cases where any exceedance of the maximum conductor temperature is unacceptable, it may be prudent to select a weather threshold that has never been exceeded based on the forecast. In addition, bias correction on weather-model forecasts, rather than bias correction on derating the line, could also be added to risk mitigation measures. In any method selected, however, the weather forecast average and maximum errors should be calculated and translated to the average and maximum errors in the current forecast. The weather data from the HRRR model points were used to directly calculate ampacity, and this value was directly compared to the ampacity calculated with observed weather data at the installed weather stations, shown in Figure 4, over the year-long period of interest. In Figure 17a, the comparison is shown with the median error and the upper and lower quartiles of the error over the time period. On average, the median error is 10.1 A, the lower quartile is -200.5 A, and the upper quartile is 215.4 A. It should be noted this is the agglomeration of all weather data, and that, of this data, the lowest value of the limiting span would be utilized, which should decrease the quartile span. In addition, the

average median for each month of the study is shown in Figure 17b. The largest positive differences (i.e., where the forecast ampacity would overpredict the observed ampacity) occur in January and August. In January, the relative load on this line is minor, and this would likely not have a large impact. In August, due to inoperable weather stations, this only includes 10 days, which may skew the result for this month when compared to the other months. However, August is one period of the year with high load from heating, ventilation and air conditioning systems, and further understanding the risk on this particular transmission line is especially necessary over that period. When the median is negative, as in April, then the observed ampacity would be above the forecasted ampacity, and little risk would be expected. From the utilities' business perspective, a concern could be that extra ampacity may be going unused. With a system containing installed weather stations (or other sensors) the real-time amapcity can, of course, be scaled back if the approaching forecasted weather conditions deviate from actual weather conditions as a way to mitigate risk.

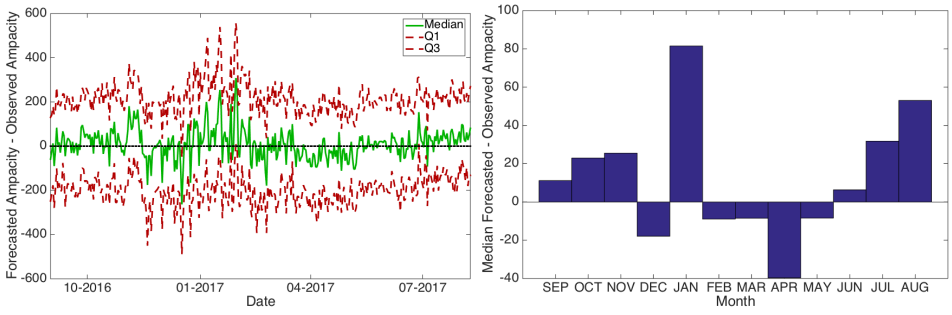

Figure 17: (a) The median and upper and lower quartile values of the ampacity for all of the HRRR to weather station comparisons, and (b) the average median of the ampacity difference in HRRR to weather station value per month.

4. Conclusion

Data from the HRRR model was extracted so that it could be used in an approach that couples with CFD wind fields. These data are then subsequently used in the GLASS software to calculate the DLR ampacity for a transmission line across southern Idaho for a year-long period of study. The error between the calculation of ampacity for the long-term (up to 18

hour) forecasts and the short-term (3-hour ahead) forecasts, using the HRRR model coupled with CFD, is relatively minor compared to the static rating of the line. This should give utilities confidence in utilizing the forecasted DLR ampacity ratings for alleviating congestion in the utility market. The data show the potential for this method to be usable by utility companies to forecast the amount of ampacity on their line for market transactions or alleviating congestion.

A conservative assumption was made on derating the line by four standard deviations of the difference between the 3-hour and 18-hour forecast. This was done as an example to alleviate risk on the system. Even with this conservative assumption, significant headroom exists for the DLR above the static rating of this line during summer months, when congestion issues are typically more problematic. Recent changes to the HRRR model expand its use up to 36 hours, and the ability to produce an ampacity prediction will likely become more advantageous as the forecasted time period is expanded. However, to fully analyze the advantage of the updated HRRR model in a similar way will take a year of new data collection.

In the future, the model comparison could be coupled with direct-measurement devices using GLASS on the transmission line of interest to increase confidence in this predictive model for DLR ampacity. Similarly, future work could include a comparison of the pure model-based approach with direct measurement data for validation. However, with NWPs, the same accuracy may not be universal across the entire area studied, and an understanding of the differences between observed and predicted weather conditions in the region of interest should be reached prior to using a pure model-based approach for DLR. If needed, installation of indirect- or direct-measurement devices along the line should be used in conjunction with the model to increase robustness.

Acknowledgments

The research was conducted by Idaho National Laboratory for the U.S. Department of Energy, Wind Energy Technology Office, in conjunction with the National Oceanic and Atmospheric Administration. Idaho National Laboratory is operated by Battelle Energy Alliance under contract No. DE AC07-05ID14517. NOAA is funded under the Department of Commerce and collaborates with CIRA through Award Number NA14OAR4320125 and CIRES through Award Number NA17OAR4320101.

Declaration of Interests

None.

References

[1] Smart Grid System Report, Technical Report, U.S. Department of Energy, 2010.

[2] Dynamic line rating systems for transmission lines: American Recovery and Reinvestment Act of 2009, Technical Report, U.S. Department of Energy, 2014.

[3] Standard for Calculating Current-Temperature Relationship of Bare Overhead Line Conductors, Technical Report, IEEE Standard 738, 2012.

[4] IEEE PES WG Subcommittee 15.11, Real-time overhead transmission line monitoring for dynamic rating, IEEE Trans. Power Deliv. 31 (2016).

[5] Guide for selection of weather parameters for bare overhead conductor ratings, Technical Report, CIGRE WG 22.12, 2006.

[6] CIGRE Working Group 22.12, The thermal behaviour of overhead line conductors, Electra 114 (1992) 107–125.

[7] Guide for thermal rating calculations of overhead lines, Technical Report, CIGRE WG B2.43, 2014.

[8] Overhead Electrical Conductors Calculation Methods for Stranded Bare Conductors, Technical Report, IEC Standard TR 1597, 1985.

[9] Transmission Facility Rating Methodology, Technical Report, Kansas City Power and Light Company, 2017.

[10] B. P. Bhattarai, J. P. Gentle, P. Hill, T. McJunkin, K. S. Myers, A. Abboud, R. Renwick, D. Hengst, Transmission line ampacity improvements of altalink wind plant overhead tie-lines using weather-based dynamic line ratings, in: IEEE PES General Meeting.

[11] B. P. Bhattarai, J. P. Gentle, T. McJunkin, P. J. Hill, K. Myers, A. Abboud, D. Hengst, Improvement of transmission line ampacity utilization by weather-based dynamic line ratings, IEEE Trans. Power Deliv. 33 (2018) 1853–1863.

[12] D. Greenwood, J. Gentle, K. Myers, P. Davison, I. West, J. Bush, G. Ingram, M. Troffaes, A comparison of real-time thermal rating systems in the u.s. and the u.k., IEEE Trans. Power Deliv. 29 (2014) 1849–1858.

[13] J. Marmillo, N. Pinney, B. Mehraban, S. Murphy, N. Dumitriu, Simulating the economic impact of a dynamic line rating project in a regional transmission operator (rto) environment, in: CIGRE U.S. National Committee 2018 Grid of the Future Symposium.

[14] A. Abboud, J. Gentle, T. McJunkin, B. Fehringer, J. Lehmer, Using computational fluid dynamics to assess dynamic line ratings in southern idaho, in: CIGRE U.S. National Committee 2018 Grid of the Future Symposium.

[15] E. Cloet, J.-L. Lilien, Uprating transmission lines through the use of an innovative real-time monitoring system, in: Transmission and Distribution Construction, Operation and Live-Line Maintenance (ESMO), 2011 IEEE PES 12th International Conference on, IEEE, pp. 1–6.

[16] F. Soto, D. Alvira, L. Martin, J. Latorre, J. Lumbreras, M. Wagensberg, Increasing the capacity of overhead lines in the 400 kv spanish transmission network: real time thermal ratings, Sesja CIGRE (1998) 22–211.

[17] D. Piccagli, M. Barbieri, M. Pozzi, G. Giannuzzi, R. Zaottini, Recent advances in wams data processing: Off-line and on-line applications for stability monitoring and dynamic loading, in: Proc. CIGRÉ Belgium Conf.

[18] S. Kim, M. M. Morcos, An application of dynamic thermal line rating control system to up-rate the ampacity of overhead transmission lines, IEEE Trans. Power Deliv. 28 (2013) 1231–1232.

[19] C. Y. Cong, P. Regulski, P. Wall, M. Osborne, V. Terzija, On the use of dynamic thermal-line ratings for improving operational tripping schemes, IEEE Trans. Power Deliv. 32 (2016) 1891–2900.

[20] E. F. Qiu, J. Wang, Distributionally robust congestion management with dynamic line rating, IEEE Trans. Power Syst. 30 (2015) 2198–2199.

[21] L. Dawson, A. Knight, Applicability of dynamic thermal line rating for long lines, IEEE Trans. Power Deliv. 33 (2018).

[22] J. Gentle, Concurrent wind cooling in power transmission lines, in: Western Energy Policy Research Conference, 2012.

[23] D. Greenwood, P. Taylor, Investing the impact of real-time thermal ratings on power network reliability, IEEE Trans. Power Syst. 23 (2014) 2460–2468.

[24] J.-A. Jiang, Y.-T. Liang, C.-P. Chen, X.-Y. Zheng, C.-L. Chuang, C.-H. Wang, On dispatching line ampacities of power grids using weather-based conductor temperature forecasts, IEEE Trans. Smart Grid 9 (2018).

[25] T. B. Phillips, I. Senocak, J. P. Gentle, M. K. S., Anderson, Investigation of a dynamic power line rating concept for improved wind energy integration over complex terrain, in: ASME 2014 4th Joint US-European Fluids Engineering Division Summer Meeting.

[26] T. Phillips, Dynamic rating of transmission lines for improved wind energy integration in complex terrain, Master's thesis, Boise State University, 2014.

[27] G. C. J. Wallnerstrom, Y. Huang, L. Soder, Impact from dynamic line rating on wind power integration, IEEE Trans. Smart Grid 6 (2015) 343–350.

[28] L. Bird, J. Cochran, X. Wang, Wind and solar energy curtailment: Experience and practices in the united states, 2014.

[29] S. Uski-Joutsenvuo, R. Pasonen, Maximizing power line transmission capability by employing dynamic line ratings technical survey and applicability in Finland, VTT-R-01604-13, Technical Report, 2013.

[30] C. R. Black, W. A. Chisholm, Key considerations for the selection of dynamic thermal line rating systems, IEEE Trans. Power Deliv. 30 (2015) 2154–2162.

[31] A. Dino, A. Ketly, Dynamic Transmission Line Rating: Technology Review, Technical Report, Hydro Tasmania Consulting, 208478-CR-001, 2009.

[32] S. Karimi, P. Musilek, A. M. Knight, Dynamic thermal rating of transmission lines: A review, Renew. Sustain. Energy Rev. 91 (2018) 600–612.

[33] A. Babs, Weather-based and conductor state measurement methods applied for dynamic line rating forecasting, in: International Conference on Advanced Power System Automation and Protection (APAP), 2011, volume 1, IEEE, pp. 762–765.

[34] E. Carlini, C. Pisani, A. Vaccaro, D. Villacci, A reliable computing framework for dynamic line rating of overhead lines, Elect. Power Syst. Res. 132 (2016) 1–8.

[35] C. Pisani, A. Vaccaro, D. Villacci, Dynamic line rating of overhead lines by cooperative and self-organizing sensor networks, in: 2015 AEIT International Annual Conference (AEIT), 14-16 Oct. 2015, Naples Italy.

[36] C. Pisani, A. Vaccaro, D. Villacci, Conceptualization and experimental deployment of an adaptive synchronized sensing system for power line thermal monitoring., IEEE Trans. Ind. Inform. 12 (2016) 2158–2165.

[37] E. M. Carlini, C. Pisani, A. Vaccaro, D. Villacci, Dynamic line rating monitoring in wams: Challenges and practical solutions, in: 2015 IEEE 1st International Forum on Research and Technologies for Society and Industry Leveraging a better tomorrow (RTSI), 16-18 Sept. 2015, Turin, Italy.

[38] B. Clairmont, D. Douglas, J. Inglesias, Z. Peter, Radial and longitudinal temperature gradients in bare stranded conductors with high current densities, Paris: Cigre (2012).

[39] A. Phillips, Evaluation of instrumentation and dynamic thermal ratings for overhead lines, Technical Report, New York Power Authority, White Plains, NY (United States), 2013.

[40] M. A. Bucher, G. Andersson, Robust corrective control measures in power systems with dynamic line rating, IEEE Trans. Power Syst. 31 (2016) 2034–2043.

[41] D.-M. Kim, J.-M. Cho, H.-S. Lee, H.-S. Jung, J.-O. Kim, Prediction of dynamic line rating based on assessment risk by time series weather

model, in: International Conference on Probabilistic Methods Applied to Power Systems, 2006. PMAPS 2006., IEEE, pp. 1–7.

[42] X. Sun, P. B. Luh, K. W. Cheung, W. Guan, Probabilistic forecasting of dynamic line rating for over-head transmission lines, in: Power & Energy Society General Meeting, 2015 IEEE, IEEE, pp. 1–5.

[43] A. Michiorri, H. Nguen, S. Allessandrini, J. Bremnes, S. Dierer, E. Ferrero, B. Nygaard, P. Pinson, N. Thomaidis, S. Uski, Forecasting for dynamic line rating, Renew. Sustain. Energy Rev. 52 (2015) 1713–1730.

[44] S. Uski, Dynamic line rating forecastability for conservative day-ahead line rating values, in: Industrial Electronics Society, IECON 2015-41st Annual Conference of the IEEE, IEEE, pp. 003738–003742.

[45] T. Ringelband, P. Schäfer, A. Moser, Probabilistic ampacity forecasting for overhead lines using weather forecast ensembles, Elect. Eng. 95 (2013) 99–107.

[46] R. Dupin, A. Michiorri, G. Kariniotakis, Dynamic line rating day-ahead forecasts - cost benefit based selection of the optimal quantile, in: CIRED 2016 Workshop Electrical networks for society and people, Jun 2016, Helsinki, Finland.

[47] B. J. L. Aznarte, N. Siebert, Dynamic line rating using numerical weather predictions and machine learning: A case study, IEEE Trans. Power Deliv. 32 (2017) 335–343.

[48] W. Jones, B. Launder, The prediction of laminarization with a two-equation model of turbulence, Int. J. Heat Mass Transf. 15 (1972) 301–314.

[49] T. Wallbank, WindSim Validation Study: CFD Validation in Complex Terrain, Technical Report, 2008.

[50] A. Dhunny, M. Loolchund, S. Rughooputh, Numerical analysis of wind flow patterns over complex hilly terrains: comparison between two commonly used cfd software, Int. J. Glob. Energy Issues 39 (2016) 181–203.

[51] S. Milashuk, W. Crane, Wind speed prediction accuracy and expected errors of rans equations in low relief inland terrain for wind resource assessment purposes, Enviro. Model. Softw. 26 (2011) 429–433.

[52] A. Dhunny, M. Loolchund, S. Rughooputh, A high-resolution mapping of wind energy potentials for mauritus using computational fluid dynamics, Wind Struct. 20 (2015) 565–578.

[53] A. Dhunny, M. Loolchund, S. Rughooputh, Wind energy evaluation for a highly complex terrain using computational fluid dynamics (cfd), Renew. Energy 101 (2017) 1–9.

[54] T. Smith, S. Benjamin, J. Brown, S. Weygandt, T. Smirnova, B. Schwartz, Convection forecasts from the hourly updated, 3-km high resolution rapid refresh (hrrr) model., in: 24th Conference on Severe Local Storms, Savanah, GA, 2008.

[55] S. G. Benjamin, S. S. Weygandt, J. M. Brown, M. Hu, C. R. Alexander, T. G. Smirnova, J. B. Olson, E. P. James, D. C. Dowell, G. A. Grell, et al., A north american hourly assimilation and model forecast cycle: The rapid refresh, Mon. Weather Rev. 144 (2016) 1669–1694.